nature nanotechnology

ARTICLES

https://doi.org/10.1038/s41565-022-01113-4

Exploiting the full advantages of colloidal perovskite nanocrystals for large-area efficient light-emitting diodes

Young-Hoon Kim[1,2,5], Jinwoo Park[1,5], Sungjin Kim[1,5], Joo Sung Kim[1], Hengxing Xu[3], Su-Hun Jeong[1], Bin Hu[3] and Tae-Woo Lee[1,4] ✉

Cost-effective, high-throughput industrial applications of metal halide perovskites in large-area displays are hampered by the fundamental difficulty of controlling the process of polycrystalline film formation from precursors, which results in the random growth of crystals, leading to non-uniform large grains and thus low electroluminescence efficiency in large-area perovskite light-emitting diodes (PeLEDs). Here we report that highly efficient large-area PeLEDs with high uniformity can be realized through the use of colloidal perovskite nanocrystals (PNCs), decoupling the crystallization of perovskites from film formation. PNCs were precrystallized and surrounded by organic ligands, and thus they were not affected by the film formation process, in which a simple modified bar-coating method facilitated the evaporation of residual solvent to provide uniform large-area films. PeLEDs incorporating the uniform bar-coated PNC films achieved an external quantum efficiency (EQE) of 23.26% for a pixel size of 4 mm² and an EQE of 22.5% for a large pixel area of 102 mm² with high reproducibility. This method provides a promising approach towards the development of large-scale industrial displays and solid-state lighting using perovskite emitters.

Metal halide perovskites have many outstanding optoelectronic properties, such as high absorption coefficients, narrow emission spectra (full-width at half-maximum (FWHM) ≈ 20 nm), tunable emission wavelengths (400 nm ≤ λ ≤ 780 nm) and high charge carrier mobility[1–5]. Perovskites are composed of low-cost elements and are solution-processable[6], and therefore they are being developed as light-harvesting materials and light emitters that can be mass-produced to achieve the commercialization of large-size solar cells, displays and solid-state lighting. These developments have led to perovskite solar cells (PSCs) with high power conversion efficiencies (25.4%)[7] and perovskite light-emitting diodes (PeLEDs) with high electroluminescence (EL) efficiencies (external quantum efficiency (EQE) = 23.4%, current efficiency (CE) = 108 cd A^{-1})[8].

Most of the research on high-efficiency PSCs and PeLEDs has focused on the spin coating of polycrystalline films[9–15]. Unlike PSCs, polycrystalline film-based PeLEDs have non-uniform and poor device performance over large areas due to the intrinsic limitations of (1) controlled crystal growth of perovskite polycrystalline films and (2) achieving small grains to have sufficient charge carrier confinement. Furthermore, the spin coating of polycrystalline films involves sequential crystallization steps: the deposition of a wet precursor solution, evaporation of solvent during spin coating, and nucleation and growth of crystals[16]. This process often includes an additional process, called nanocrystal pinning, to achieve uniform and small nanograins[5], which complicates the crystallization process. These multiple steps are closely related to each other and substantially affected by small variations in fabrication conditions (for example, atmosphere, temperature, surface energy of the substrates and nanocrystal pinning time), so the experimental conditions to achieve the best efficiency may be different, depending on the environments in laboratories that do not have well-controlled dry rooms. Moreover, this process is limited to small areas[17]; when applied to a large area, non-uniform films are formed[16], which limits EL efficiency, reproducibility, uniformity and the mass production of large-area PeLEDs[18].

Printing processes that can fabricate large-area perovskite polycrystalline films have been developed for the mass production mostly of PSCs[17]. However, uniform perovskite polycrystalline thin films (thickness <50 nm) with small nanograins (Supplementary Fig. 1), which are required to achieve optimum light outcoupling[19] and the confinement of charge carriers[5] in efficient PeLEDs, cannot be easily fabricated by these printing methods. Because of the fundamental nature of halide perovskites, which possess low exciton binding energy and long diffusion length for both holes and electrons, printed non-uniform and thick polycrystalline films with large grain size are much more detrimental to achieving high EL efficiency and reproducibility in large-area PeLEDs than in PSCs, which exploit the advantages of large grains and thick films. Therefore, research into printing perovskite polycrystalline films has mainly focused on photovoltaics rather than light-emitting diode (LED) applications[17].

Recently, near-infrared PeLEDs incorporating blade-coated methylammonium lead iodide ($MAPbI_3$) polycrystalline films were developed to achieve a decent EQE of 16.1% for a pixel size of 4 mm², but they showed reduced EQE for a large pixel size (12.7% in 100 mm²) due to the difficulty of controlling the crystallization of perovskite polycrystalline films over a large area[16]. Furthermore, the film morphology was still substantially affected by blade-coating speed, temperature and N_2 knife pressure, which is an additional

[1]Department of Materials Science and Engineering, Seoul National University, Seoul, Republic of Korea. [2]Department of Energy Engineering, Hanyang University, Seoul, Republic of Korea. [3]Department of Materials Science and Engineering, University of Tennessee, Knoxville, TN, USA. [4]School of Chemical and Biological Engineering, Institute of Engineering Research, Research Institute of Advanced Materials, Soft Foundry, Seoul National University, Seoul, Republic of Korea. [5]These authors contributed equally: Young-Hoon Kim, Jinwoo Park, Sungjin Kim. ✉e-mail: twlees@snu.ac.kr

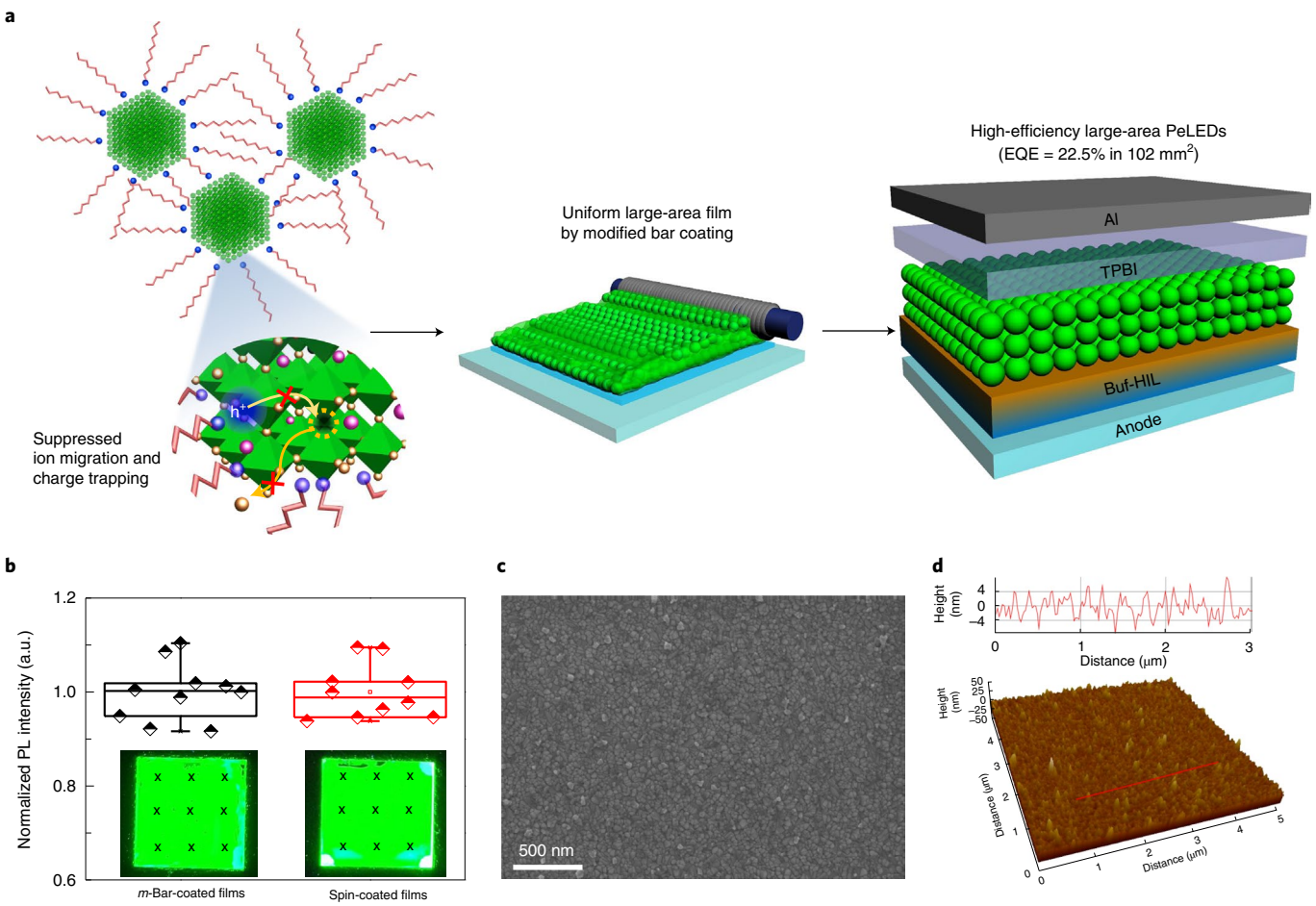

Fig. 1 | Characteristics of colloidal PNCs for large-area bar-coated PeLEDs. a, Schematic illustration of the suppression of charge trapping and ion migration (left), fabrication of uniform PNC films by *m*-bar coating (middle) and device structure of high-efficiency large-area PeLEDs based on *m*-bar-coated PNC films (right). **b**, Normalized PL intensity of *m*-bar-coated and spin-coated PNC films (measured at the points marked by a cross in the inset). In the box plots, the top and bottom whiskers are the maximum and minimum values of the data, respectively, the upper and lower horizontal lines in the boxes indicate the upper quartile and lower quartile, respectively, and the middle horizontal lines in the boxes are median values. **c**,**d**, Scanning electron microscopy image (**c**) and atomic force microscopy image (bottom) and cross-sectional roughness (top) (**d**) of *m*-bar-coated PNC films. The top plot in **d** indicates the height profile of the red line in the surface profile image (bottom). The grey lines in the top plot in **d** represent equivalent surface height.

process[16]. These drawbacks make it difficult to transfer the process to other scalable manufacturing lines to achieve large-area and high-throughput production. This implies that large-area PeLED devices for mass production should be fabricated using materials that are not severely affected by processing conditions and environment.

Here we propose that the conventional problems of poor EL efficiency and non-uniformity in large-area PeLEDs can be overcome by printing colloidal perovskite nanocrystals (PNCs) using a modified bar-coating (*m*-bar-coating) method that allows for the fast evaporation of residual solvent. *m*-Bar-coated PNC films substantially reduce the drop in EL efficiency of bar-coated large-area PeLEDs compared with spin-coated small-area PeLEDs (Fig. 1a). In our PNC films, surface-capping organic ligands effectively suppress ion migration and charge trapping during the operation of PeLEDs, which was confirmed by low capacitance at low frequency, magnetic field-independent photoluminescence (PL) and the absence of overshoot in transient EL. Unlike the conventional approach in which polycrystalline bulk films crystallize during film formation[9–16], precrystallization along with ligand-mediated solvation of PNCs in non-polar solvents[20] and fast solvent evaporation through *m*-bar coating provide a crystal structure that is not affected by the film formation process and forms uniform large-area PNC films; the uniformity of the PNC films formed by *m*-bar coating is similar to that obtained by spin coating (Fig. 1b–d and Supplementary Figs. 2–5). Using these *m*-bar-coated PNC films, we achieved EQE = 23.26% in PeLEDs with a pixel size of 4 mm^2 and EQE = 22.5% in large-area PeLEDs with a pixel size of 102 mm^2, with both types of PeLEDs showing high reproducibility. We have also demonstrated bright and uniform PeLEDs that maintained a high EQE of 21.46% for an area of 900 mm^2.

Suppressed ion migration and charge trapping in PNC films

Colloidal PNCs were synthesized using a simple solubility-difference-assisted recrystallization method at room temperature in air[8,21] instead of by the hot-injection method at high temperature (>150 °C)[22]. The as-synthesized colloidal formamidinium lead bromide ($FAPbBr_3$) PNCs had predominantly circular shapes with an average diameter of ~9.63 nm (Supplementary Fig. 6). To maintain organic ligands on the surfaces of the as-synthesized PNCs, we did not purify them using anti-solvent (for example, methyl acetate, which is standard for the purification of colloidal PNCs)[22,23]. Instead, we changed the solvent in the as-synthesized PNCs to pure toluene for device fabrication (see Methods for details), which allows high device efficiency without serious hindrance to charge carrier transport in the PNC films. The X-ray photoelectron

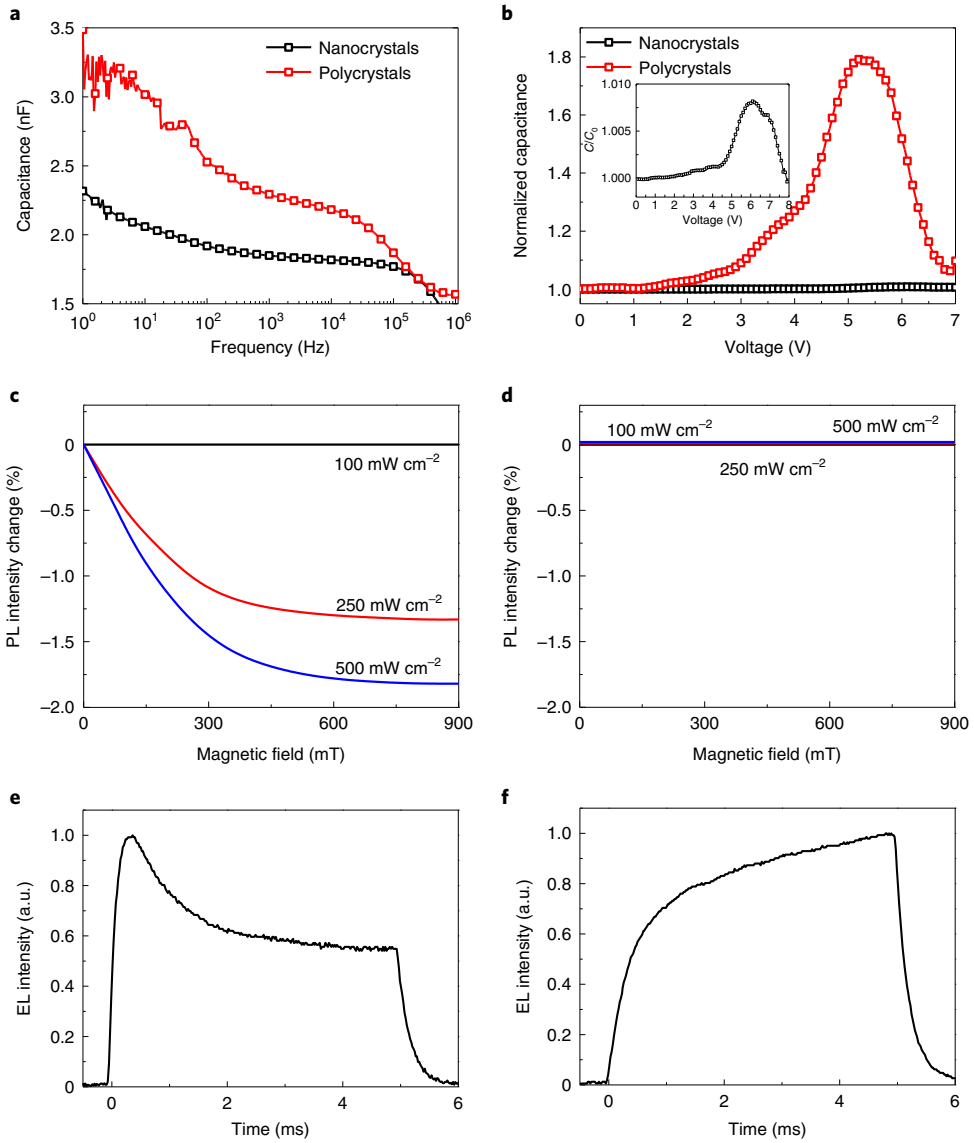

Fig. 2 | Suppressed ion migration and charge trapping in PNC films. a,**b**, *C*–*f* (**a**) and normalized *C*–*V* (**b**) characteristics of PeLEDs fabricated with $FAPbBr_3$ polycrystalline or PNC films. Inset: a magnified *C*–*V* plot of the PeLEDs comprising PNC films. **c**,**d**, Magnetic field–photoluminescence characteristics of $FAPbBr_3$ polycrystalline (**c**) and PNC (**d**) films. **e**,**f**, Transient EL characteristics of PeLEDs based on polycrystalline (**e**) and PNC (**f**) films.

spectra of the PNC films showed clear peaks of Br (~68–70 eV) and Pb (~139 and ~144 eV), which characterize the perovskite, and C (~282–285 eV), N (~400 eV) and O (~532–535 eV), which indicate the presence of organic ligands (*n*-decylamine and oleic acid) passivating the PNC surface in the films (Supplementary Fig. 7)[24]. These surface-covering organic ligands have low dielectric constants[25] and induce the efficient confinement of charge carriers inside the PNC films[24,26]. This confinement yielded higher photoluminescence quantum efficiencies (PLQE ≈ 55.8 and 56.2% in spin-coated and *m*-bar-coated films, respectively) and exciton binding energy ($E_B \approx 76$ meV; Supplementary Fig. 8) in $FAPbBr_3$ PNC films than in $FAPbBr_3$ polycrystalline films (PLQE ≈ 15% and 1% in spin-coated and *m*-bar-coated films, respectively, and $E_B \approx 25$ meV)[27].

Ion migration and charge trapping were also suppressed during the operation of PeLEDs fabricated with PNC films. To investigate these advantages of PNCs over polycrystalline films, we fabricated PeLEDs incorporating $FAPbBr_3$ PNC or polycrystalline films with the structure indium tin oxide (ITO)/buffer hole-injection layer (Buf-HIL)[4]/$FAPbBr_3$ PNC or polycrystalline film/2,2′,2″-(1,3,5-benzenetriyl)tris(1-phenyl-1*H*-benzimidazole) (TPBI)/LiF/Al and measured their capacitance at different frequencies and applied biases. To increase the uniformity of the fabricated polycrystalline films, we dropped 3–4 droplets of pure chloroform onto the quasi-film of the precursor solution during spinning (that is, nanocrystal pinning)[5], achieving a grain size of ~100–500 nm, whereas we spin-coated the PNC solutions to fabricate PNC films (particle size ~5–50 nm; Supplementary Figs. 5 and 9).

In capacitance–frequency (*C*–*f*) measurements, the PeLEDs incorporating polycrystalline films (polycrystal-PeLEDs) showed much higher capacitance than those incorporating PNC films (PNC-PeLEDs) at frequencies $<10^5$ Hz (Fig. 2a); the increase in capacitance as frequencies decreased below 10^5 Hz is related to the relaxation of ions[28,29]. The lower capacitance of the PNC-PeLEDs compared with the polycrystal-PeLEDs indicates suppressed ion migration in the PNC film; this effect is confirmed by the lower increase in capacitance of the PNC-PeLEDs compared with the polycrystal-PeLEDs in capacitance–voltage (*C*–*V*) measurements at a constant frequency of 1,000 Hz (Fig. 2b). Grain–particle boundaries act as major

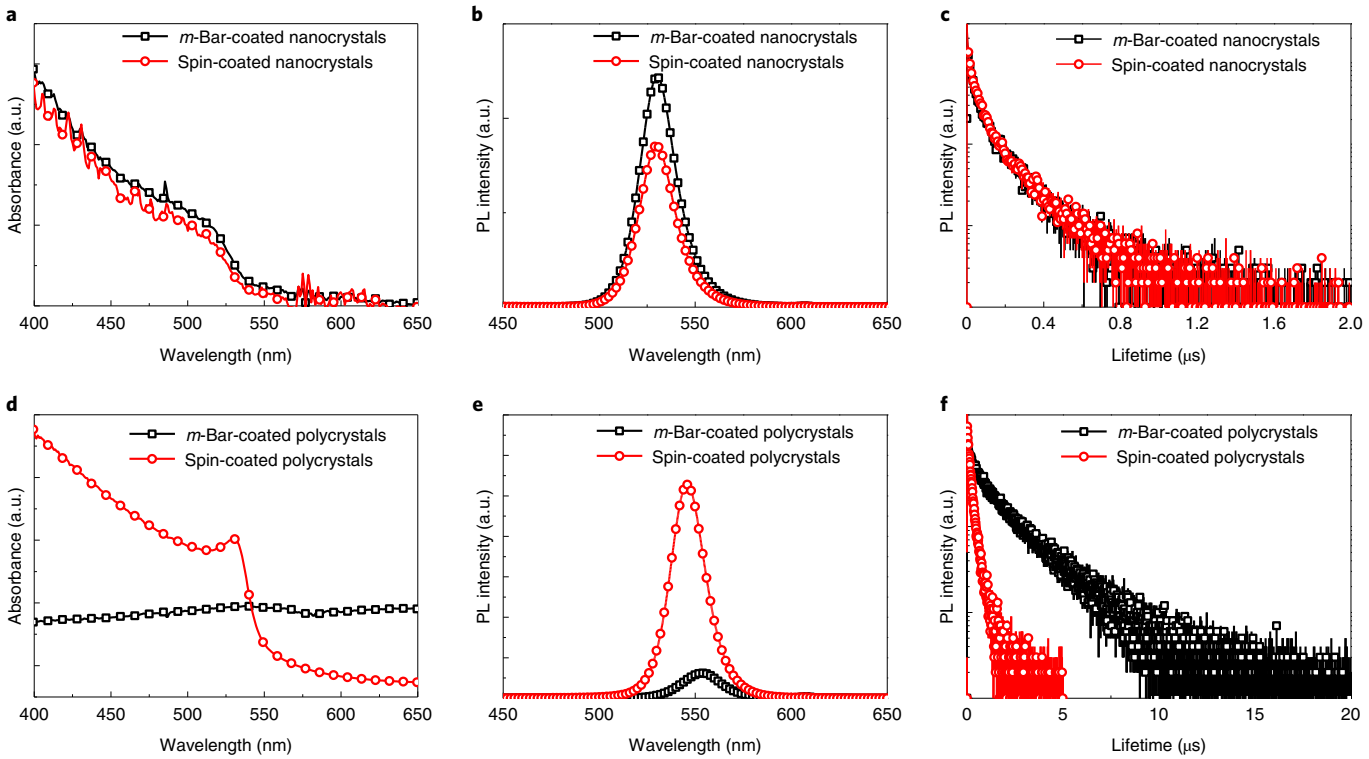

Fig. 3 | Photophysical analysis of PNC and polycrystalline films fabricated by *m*-bar coating and spin coating. a–c, Absorbance (**a**) and steady-state PL (**b**) spectra and transient PL decay curves (**c**) of PNC films fabricated by *m*-bar coating and spin coating. **d–f**, Absorbance (**d**) and steady-state PL (**e**) spectra and transient PL decay curves (**f**) of perovskite polycrystalline films fabricated by *m*-bar coating and spin coating.

ion-migration pathways[30,31], and PNC films have many more of them than do polycrystalline films due to the higher surface-to-bulk ratio of PNC films compared with polycrystalline films[32,33]. However, the PNC surface is capped with organic ligands, whereas the grains in polycrystalline films are not, so ion migration in PNC films can be suppressed by the ligands between nanocrystals in the films. The suppressed ion migration in PNC films is further confirmed by the higher activation energy (E_a) for ion migration (~0.5 eV) compared with in polycrystalline bulk films (~0.14 eV; Supplementary Fig. 10).

Furthermore, the capacitance in *C–f* measurements at low frequencies (<10^3 Hz) is normally governed by film surface polarization, which can consist of charged surface defects and surface-accumulated charged species[34]. Therefore, the lower capacitance amplitude of the PNC-PeLEDs at low frequency indicates that PNC films have a high-quality surface with largely suppressed charged surface defects and surface-accumulated charged species compared with polycrystal-PeLEDs (Fig. 2a).

To further study the effects of increased exciton binding energy and suppressed charge trapping on the PL of PNC films, we also measured the PL intensity of $FAPbBr_3$ PNC and polycrystalline films as a function of applied magnetic field (0–900 mT) under photoexcitation (intensity, 100, 250 and 500 mW cm^{-2}). Photoexcitation at >100 mW cm^{-2} led to a gradual decrease in the PL intensity of $FAPbBr_3$ polycrystalline films as the magnetic field strength increased (Fig. 2c). In contrast, the PL intensity of $FAPbBr_3$ PNC films was not affected by magnetic field upon photoexcitation, revealing the absence of magnetic field effects on PL (Fig. 2d). This implies that electron–hole pairs are formed in PNC films with a stronger binding energy and exchange interaction, ruling out perturbation of conversion between bright and dark states upon application of a magnetic field (Supplementary Text 1)[35–39]. This provides direct evidence that the strong carrier confinement and suppressed defects within the PNC structures generate high PLQE of the light-emitting excitons.

To investigate the effects of organic ligands on charge trapping during device operation, we compared the transient EL of $FAPbBr_3$ polycrystal- and PNC-PeLEDs. The polycrystal-PeLEDs showed luminance overshoot that saturated at 0.5 ms, which then decreased to a steady value (intensity ~60% of luminance overshoot; Fig. 2e), whereas the PNC-PeLEDs showed no overshoot (Fig. 2f). In transient EL, luminance overshoot generally occurs as a result of recombination between pretrapped charge carriers and injected charge carriers[40,41]. After most of the pretrapped charge carriers have recombined with the injected charge carriers, luminance occurs only as a result of recombination between injected charge carriers, so luminance gradually decreases to a steady state[40,41]. Therefore, the transient EL data indicate that the organic surface ligands in PNC films efficiently passivate defects and prevent charge carrier trapping during the operation of PeLEDs.

An increase in applied bias had different effects on the polycrystal- and PNC-PeLEDs. In the polycrystal-PeLEDs, the EL increased to a maximum overshoot intensity ($I_{EL,over}$) in ~0.5 ms, then decayed to a steady-state intensity ($I_{EL,ss}$) at ~5 ms, and the ratio $I_{EL,ss}/I_{EL,over}$ increased from ~0.52 at 3.8 V to ~0.77 at 5 V. In contrast, in the PNC-PeLEDs, an increase in applied bias accelerated the rise time (t_s) required to reach ~90% saturated EL intensity from ~3.29 ms at 3.4 V to ~1.61 ms at 5 V (Supplementary Fig. 11).

Fabrication of uniform, large-area PNC films by modified bar coating

To explore whether PNC film morphology is affected by the film formation process, we compared $FAPbBr_3$ PNC and polycrystalline films fabricated by spin coating and *m*-bar coating. For the *m*-bar coating of PNC and polycrystalline films, we held the substrate at an angle of ≥50° with respect to the surface immediately after bar coating of the perovskite solution to evaporate the remaining solvent (schematic illustrations and the mechanism of *m*-bar coating are shown in

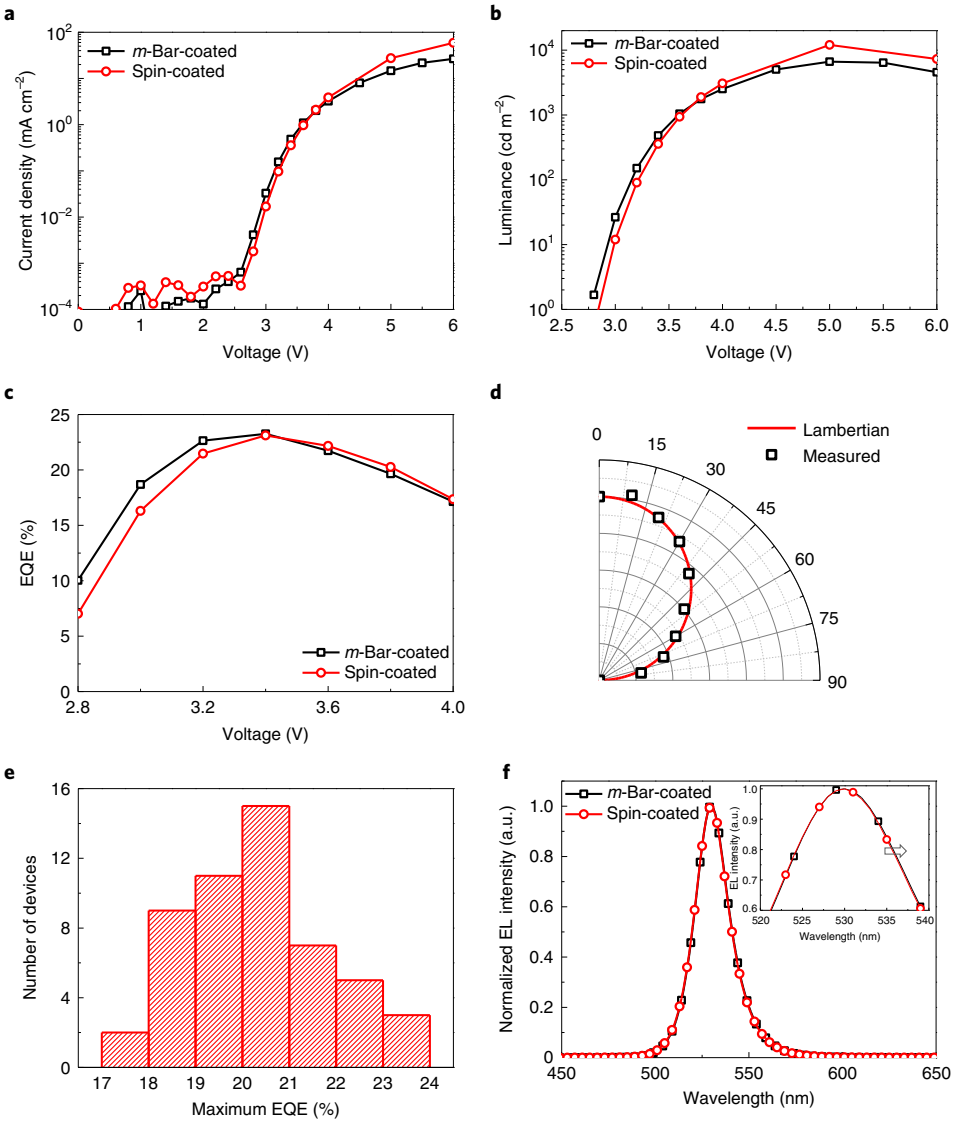

Fig. 4 | Characteristics of $FA_{0.875}GA_{0.125}PbBr_3$ PNC-PeLEDs. a–c, Current densities (**a**), luminances (**b**) and EQEs (**c**) of $FA_{0.875}GA_{0.125}PbBr_3$ PNC-PeLEDs based on PNC films fabricated by spin coating and *m*-bar coating. **d**,**e**, Angular intensity profiles (**d**) and EQE histogram (**e**) of $FA_{0.875}GA_{0.125}PbBr_3$ PNC-PeLEDs fabricated using *m*-bar-coated PNC films. **f**, EL spectrum (inset: magnified image) of $FA_{0.875}GA_{0.125}PbBr_3$ PNC-PeLEDs using PNC films fabricated by spin coating and *m*-bar coating.

Supplementary Figs. 12 and 13)[42]. The PNC films fabricated by *m*-bar coating showed highly uniform surface roughness, PL intensity, absorption and PL lifetime over a large area ($3\times3\,cm^2$), which were comparable to the spin-coated PNC films (Fig. 3a–c and Supplementary Figs. 2–5). The absorption and PL intensities were slightly higher in the *m*-bar-coated PNC films than in the spin-coated PNC films owing to their slightly greater thickness (~33 nm compared with ~25 nm, respectively). The *m*-bar-coated PNC film-based PeLEDs also showed similar capacitance to the spin-coated PNC film-based PeLEDs in *C–f* measurements (Fig. 2a, Supplementary Fig. 14 and associated discussion). However, PNC films fabricated by conventional bar coating without tilting of the substrate showed large variations in the PL and absorption spectra over a large area (Supplementary Figs. 15 and 16)[43]. The uniformity of the *m*-bar-coated PNC films increased with tilting angle and saturated at a tilting angle of ≥50° (see Supplementary Fig. 17 and associated discussion for more details).

m-Bar-coated polycrystalline films without any further additional processing showed (1) an absorption spectrum that could not be measured, (2) a redshifted PL (peak at 553 nm) with substantially reduced intensity and (3) a drastically extended PL lifetime (1,785 ns) compared with the spin-coated polycrystalline films (PL peak at 545 nm, PL lifetime of ~214.4 ns; Fig. 3d–f). These differences arise from the poor film coverage and large crystals (size >10 μm) resulting from the slow evaporation of the dimethyl sulfoxide (DMSO) solvent, which has a high boiling point (189 °C), used in the *m*-bar-coating of polycrystalline films (Supplementary Fig. 18)[5].

To understand the dynamics of charge carrier recombination in PNC and polycrystalline films fabricated by spin coating and *m*-bar coating, we calculated the recombination rate (K), radiative recombination rate (K_r) and the non-radiative recombination rate (K_{nr}) of each sample using equations (1) and (2):

$$\text{PL lifetime} = \frac{1}{K} = \frac{1}{K_{nr} + K_r}, \quad (1)$$

$$\text{PLQE} = \frac{K_r}{K_{nr} + K_r}. \quad (2)$$

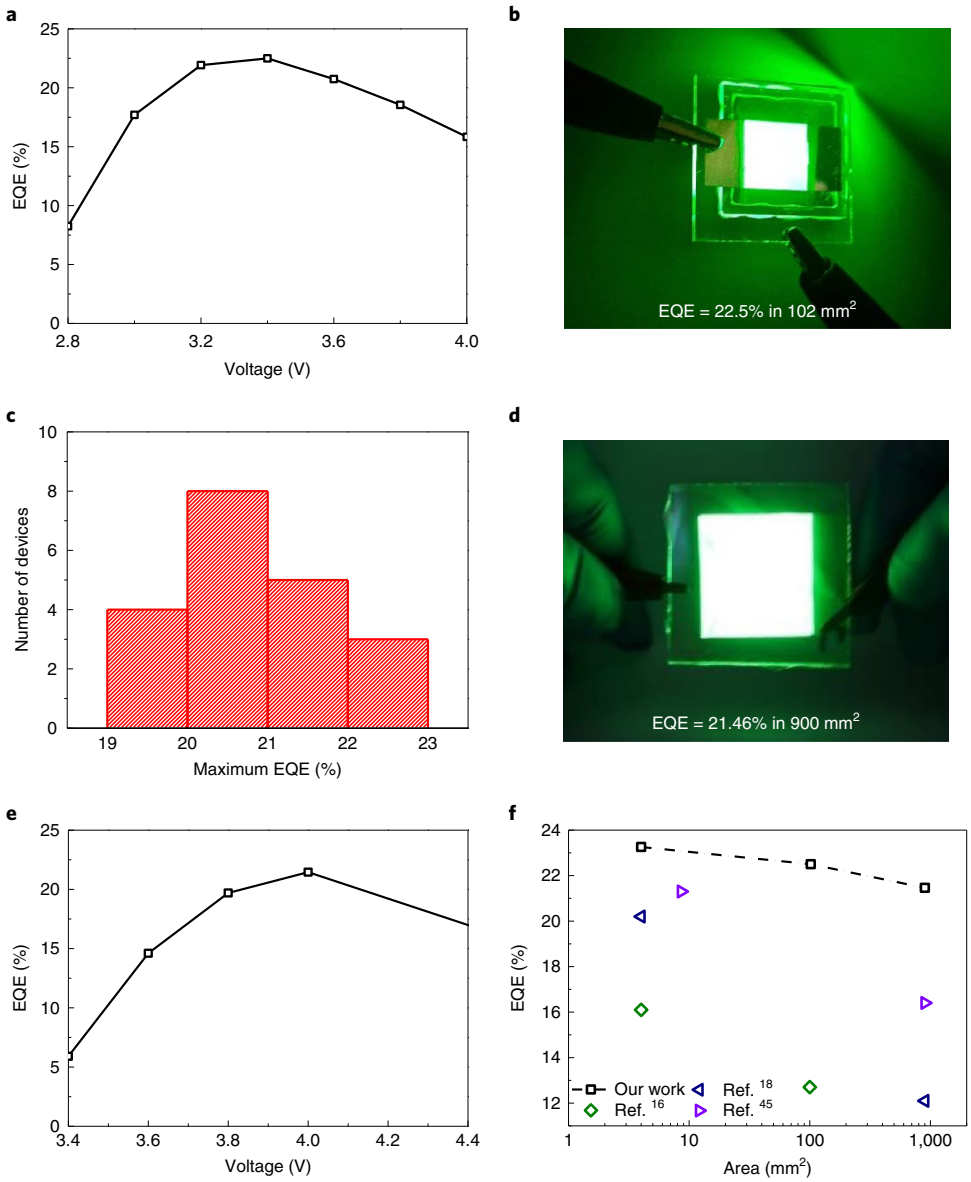

Fig. 5 | Characteristics of large-area $FA_{0.875}GA_{0.125}PbBr_3$ PNC-PeLEDs. a–c, EQEs (**a**), a photograph of an operating device (**b**) and EQE histogram (**c**) of large-area PeLEDs based on *m*-bar-coated PNC films with a pixel size of 102 mm^2. **d**,**e**, Photograph of an operating device (**d**) and EQEs (**e**) of large-area PeLEDs based on *m*-bar-coated PNC films with a pixel size of 900 mm^2. **f**, EQEs as a function of device area for PeLEDs from this work and recently reported large-area PeLEDs[16,18,45].

Polycrystalline films showed decreased K_r and K_{nr} for *m*-bar-coated films compared with spin-coated films, with K_r decreasing even more than K_{nr} ($K_r \approx 6.99\times10^5\,s^{-1}$ and $K_{nr} \approx 3.96\times10^6\,s^{-1}$ for spin-coated films, and $K_r \approx 5.6\times10^3\,s^{-1}$ and $K_{nr} \approx 5.55\times10^5\,s^{-1}$ for *m*-bar-coated films; Supplementary Table 1). In contrast, PNCs showed similar K_r and K_{nr} in both spin-coated and *m*-bar-coated films ($K_r \approx 5.53\times10^6\,s^{-1}$ and $K_{nr} \approx 4.38\times10^6\,s^{-1}$ for spin-coated films, and $K_r \approx 5.37\times10^6\,s^{-1}$ and $K_{nr} \approx 4.18\times10^6\,s^{-1}$ for *m*-bar-coated films). These results imply that the film fabrication process affects morphology and recombination dynamics in polycrystalline films but not in PNC films.

Achieving high EL efficiency in bar-coated large-area PeLEDs

Next, we investigated whether *m*-bar-coated PNC films could achieve high EL efficiency in PeLEDs. *m*-Bar-coated $FAPbBr_3$ polycrystalline films without any additional processing exhibited poor film morphology and large crystals (>10 μm), and therefore showed severe leakage current under a low applied bias (<4 V) and very low CE (6.76×10^{-5} cd A^{-1}) in polycrystal-PeLEDs compared with spin-coated $FAPbBr_3$ polycrystal-PeLEDs (CE = 5.09 cd A^{-1}; Supplementary Fig. 19). In contrast, *m*-bar-coated $FAPbBr_3$ PNC-PeLEDs achieved a high CE (71 cd A^{-1}) and EQE (15.4%) without any additional processing (Supplementary Figs. 20 and 21).

We further increased the EL efficiency of PNC-PeLEDs by adding an ~12.5% molar ratio of guanidinium ($CH_6N_3^+$, GA) to the $FAPbBr_3$ PNCs (PLQE = 90.65%) and by layering ~5 nm of 1,3,5-tris(bromomethyl)-2,4,6-triethylbenzene (TBTB) on top of the *m*-bar-coated $FA_{0.875}GA_{0.125}PbBr_3$ PNC films (Supplementary Text 2)[8]. These *m*-bar-coated $FA_{0.875}GA_{0.125}PbBr_3$ PNC-PeLEDs achieved a high EQE (23.26%) comparable to that of spin-coated $FA_{0.875}GA_{0.125}PbBr_3$ PNC-PeLEDs (23.12%; Fig. 4a–c). The EQE of *m*-bar-coated $FA_{0.875}GA_{0.125}PbBr_3$ PNC-PeLEDs was calculated by using the full angular EL distribution (Fig. 4d).

m-Bar-coated $FA_{0.875}GA_{0.125}PbBr_3$ PNC-PeLEDs showed high reproducibility in 52 devices (Fig. 4e) and sharp EL spectra (FWHM = 20 nm) with a peak at 530 nm (Fig. 4f). The slight red-shift of the EL spectrum of the *m*-bar-coated PNC-PeLEDs is due to the greater thickness of the *m*-bar-coated films (~33 nm) compared with the spin-coated films (~25 nm; inset of Fig. 4f). The device efficiency is 17 times higher than that of previously reported PeLEDs prepared with dip-coated PNC films (EQE = 1.38% for a pixel area of 5 mm^2)[44]. To the best of our knowledge, printed PNC PeLEDs have not been previously reported. PeLEDs fabricated with *m*-bar-coated PNCs combined with *m*-bar-coated TBTB or *m*-bar-coated Buf-HIL showed EQEs of 19.97 and 17.0%, respectively (see Supplementary Figs. 22 and 23 and the associated discussion for more details). These efficiencies are still higher than those of previously reported printed PeLEDs (EQE = 16.1% for PeLEDs with blade-coated perovskite polycrystalline bulk films and a spin-coated poly[*N*,*N*′-bis(4-butylphenyl)-*N*,*N*′-diphenylbenzidine] hole transport layer)[16].

To further demonstrate the possible utility of our PNCs in displays and solid-state lighting in large-scale industrial production, we fabricated large-area PeLEDs using *m*-bar coating. The *m*-bar-coated PNC-PeLEDs maintained a high EQE of 22.5% for a large pixel area of 102 mm^2 with high reproducibility in 20 devices (Fig. 5a–c), which is greatly improved compared with the previously reported large-area PeLEDs that incorporated blade-coated $MAPbI_3$ polycrystalline films (EQE = 12.7% in 100 mm^2)[16]. We also demonstrated bright and uniform PeLEDs with a pixel area of 900 mm^2 that maintained a high EQE of 21.46% (Fig. 5d,e), which is much higher than the previously reported large-area PeLEDs that incorporated spin-coated quasi-two-dimensional polycrystalline films[45] (EQE = 16.4% in 900 mm^2; Fig. 5f and Supplementary Tables 2 and 3). PeLEDs based on *m*-bar-coated $FA_{0.875}GA_{0.125}PbBr_3$ PNC films also showed similar device operating lifetime in different pixel areas (time until the initial luminance at 100 cd m^{-2} drops to 50%, T_{50} = 64 min for 4 mm^2, 56 min for 17 mm^2, 81 min for 75 mm^2, 79 min for 102 mm^2, 61 min for 200 mm^2 and 60 min for 900 mm^2) due to the uniform morphology of the *m*-bar-coated large-area $FA_{0.875}GA_{0.125}PbBr_3$ PNC films, showing substantial improvement compared with the previously reported large-area PeLEDs that used $FAPbBr_3$-based PNCs (T_{50} at 14.2 cd m^{-2} = 32 min; Supplementary Fig. 24).

Conclusions

We have achieved highly efficient, large-area PeLEDs by printing colloidal PNCs using an *m*-bar-coating process. The results indicate that colloidal PNCs are more suitable than polycrystalline films for demonstrating printed large-area, high-efficiency PeLEDs because (1) organic ligands in the PNCs prevent ion migration and charge trapping in films during the operation of PeLEDs, (2) the photophysical and morphological properties of the PNC films are not affected by the film fabrication process or conditions and (3) uniform large-area PNC films without pin holes can be easily printed by *m*-bar coating, which allows for the fast evaporation of residual solvent. We achieved an EQE of 23.26% in PeLEDs with a pixel area of 4 mm^2, and an EQE of 22.5% in an area of 102 mm^2, both of which were highly reproducible. These efficiencies represent a more than 10^6-fold improvement over polycrystal-PeLEDs fabricated by the same *m*-bar-coating process. To the best of our knowledge, our work is the first demonstration of PeLEDs that use printed PNC films. We have also demonstrated that the PeLEDs fabricated with printed PNC films maintained a high EQE of 21.46% in an area of 900 mm^2, which suggests a step towards the development of perovskite emitters in industrial displays and solid-state lighting.

Online content

Any methods, additional references, Nature Research reporting summaries, source data, extended data, supplementary information, acknowledgements, peer review information; details of author contributions and competing interests; and statements of data and code availability are available at https://doi.org/10.1038/s41565-022-01113-4.

Received: 10 April 2021; Accepted: 2 March 2022;
Published online: 16 May 2022

References

1. Kim, Y.-H., Cho, H. & Lee, T.-W. Metal halide perovskite light emitters. *Proc. Natl Acad. Sci. USA* **113**, 11694–11702 (2016).
2. Park, M.-H. et al. Boosting efficiency in polycrystalline metal halide perovskite light-emitting diodes. *ACS Energy Lett.* **4**, 1134–1149 (2019).
3. Tan, Z.-K. et al. Bright light-emitting diodes based on organometal halide perovskite. *Nat. Nanotechnol.* **9**, 687–692 (2014).
4. Kim, Y.-H. et al. Multicolored organic/inorganic hybrid perovskite light-emitting diodes. *Adv. Mater.* **27**, 1248–1254 (2015).
5. Cho, H. et al. Overcoming the electroluminescence efficiency limitations of perovskite light-emitting diodes. *Science* **350**, 1222–1225 (2015).
6. Jean, J. et al. Synthesis cost dictates the commercial viability of lead sulfide and perovskite quantum dot photovoltaics. *Energy Environ. Sci.* **11**, 2295–2305 (2018).
7. Yoo, J. J. et al. Efficient perovskite solar cells via improved carrier management. *Nature* **590**, 587–593 (2021).
8. Kim, Y.-H. et al. Comprehensive defect suppression in perovskite nanocrystals for high-efficiency light-emitting diodes. *Nat. Photon.* **15**, 148–155 (2021).
9. Xiao, Z. et al. Efficient perovskite light-emitting diodes featuring nanometre-sized crystallites. *Nat. Photon.* **11**, 108–115 (2017).
10. Yuan, M. et al. Perovskite energy funnels for efficient light-emitting diodes. *Nat. Nanotechnol.* **11**, 872–877 (2016).
11. Yang, X. et al. Efficient green light-emitting diodes based on quasi-two-dimensional composition and phase engineered perovskite with surface passivation. *Nat. Commun.* **9**, 570 (2018).
12. Lin, K. et al. Perovskite light-emitting diodes with external quantum efficiency exceeding 20 per cent. *Nature* **562**, 245–248 (2018).
13. Xu, W. et al. Rational molecular passivation for high-performance perovskite light-emitting diodes. *Nat. Photon.* **13**, 418–424 (2019).
14. Zhao, B. et al. High-efficiency perovskite–polymer bulk heterostructure light-emitting diodes. *Nat. Photon.* **12**, 783–789 (2018).
15. Dong, Y. et al. Bipolar-shell resurfacing for blue LEDs based on strongly confined perovskite quantum dots. *Nat. Nanotechnol.* **15**, 668–674 (2020).
16. Chu, S. et al. Large-area and efficient perovskite light-emitting diodes via low-temperature blade-coating. *Nat. Commun.* **12**, 147 (2021).
17. Zeng, L. et al. Controlling the crystallization dynamics of photovoltaic perovskite layers on larger-area coatings. *Energy Environ. Sci.* **13**, 4666–4690 (2020).
18. Zhao, X. & Tan, Z.-K. Large-area near-infrared perovskite light-emitting diodes. *Nat. Photon.* **14**, 215–218 (2020).
19. Zhao, L., Lee, K. M., Roh, K., Khan, S. U. Z. & Rand, B. P. Improved outcoupling efficiency and stability of perovskite light-emitting diodes using thin emitting layers. *Adv. Mater.* **31**, 1805836 (2019).
20. Kim, Y.-H. et al. Chiral-induced spin selectivity enables a room-temperature spin light-emitting diode. *Science* **371**, 1129–1133 (2021).
21. Zhang, F. et al. Brightly luminescent and color-tunable colloidal $CH_3NH_3PbX_3$ (X = Br, I, Cl) quantum dots: potential alternatives for display technology. *ACS Nano* **9**, 4533–4542 (2015).
22. Swarnkar, A. et al. Quantum dot-induced phase stabilization of α-$CsPbI_3$ perovskite for high-efficiency photovoltaics. *Science* **354**, 92–95 (2016).
23. Kim, Y.-H. et al. Strategies to achieve high circularly polarized luminescence from colloidal organic–inorganic hybrid perovskite nanocrystals. *ACS Nano* **14**, 8816–8825 (2020).
24. Kim, Y.-H., Wolf, C., Kim, H. & Lee, T.-W. Charge carrier recombination and ion migration in metal-halide perovskite nanoparticle films for efficient light-emitting diodes. *Nano Energy* **52**, 329–335 (2018).
25. Saeten, J. O., Sjoblom, J. & Gestblom, B. A dielectric spectroscopic study of fatty acid/amine complexes in solution. *J. Phys. Chem.* **95**, 1449–1453 (1991).
26. Kumar, S. et al. Ultrapure green light-emitting diodes using two-dimensional formamidinium perovskites: achieving recommendation 2020 color coordinates. *Nano Lett.* **17**, 5277–5284 (2017).
27. Galkowski, K. et al. Determination of the exciton binding energy and effective masses for methylammonium and formamidinium lead tri-halide perovskite semiconductors. *Energy Environ. Sci.* **9**, 962–970 (2016).
28. Wilson, J. N., Frost, J. M., Wallace, S. K. & Walsh, A. Dielectric and ferroic properties of metal halide perovskites. *APL Mater.* **7**, 010901 (2019).

29. Li, W. et al. Relationship of giant dielectric constant and ion migration in $CH_3NH_3PbI_3$ single crystal using dielectric spectroscopy. *J. Phys. Chem. C* **124**, 13348–13355 (2020).
30. Shao, Y. et al. Grain boundary dominated ion migration in polycrystalline organic–inorganic halide perovskite films. *Energy Environ. Sci.* **9**, 1752–1759 (2016).
31. Yuan, Y. & Huang, J. Ion migration in organometal trihalide perovskite and its impact on photovoltaic efficiency and stability. *Acc. Chem. Res.* **49**, 286–293 (2016).
32. Kim, Y.-H. et al. Highly efficient light-emitting diodes of colloidal metal–halide perovskite nanocrystals beyond quantum size. *ACS Nano* **11**, 6586–6593 (2017).
33. Kim, Y.-H. et al. High efficiency perovskite light-emitting diodes of ligand-engineered colloidal formamidinium lead bromide nanoparticles. *Nano Energy* **38**, 51–58 (2017).
34. Yang, Q. et al. Surface polarization and recombination in organic–inorganic hybrid perovskite solar cells based on photo- and electrically induced negative capacitance studies. *Org. Electron.* **62**, 203–208 (2018).
35. Hsiao, Y.-C., Wu, T., Li, M. & Hu, B. Magneto-optical studies on spin-dependent charge recombination and dissociation in perovskite solar cells. *Adv. Mater.* **27**, 2899–2906 (2015).
36. Sercel, P. C. et al. Exciton fine structure in perovskite nanocrystals. *Nano Lett.* **19**, 4068–4077 (2019).
37. Rossi, D. et al. Size-dependent dark exciton properties in cesium lead halide perovskite quantum dots. *J. Chem. Phys.* **153**, 184703 (2020).
38. Belyavsky, V. I., Levin, M. N. & Olson, N. J. Defect-induced lattice magnetism: phenomenology of magnetic-field-stimulated defect reactions in nonmagnetic solids. *Phys. Rev. B* **73**, 054429 (2006).
39. Zhang, J., Qin, J., Wu, T. & Hu, B. Doping induced orbit–orbit interaction between excitons while enhancing photovoltaic performance in tin perovskite solar cells. *J. Phys. Chem. Lett.* **11**, 6996–7001 (2020).
40. Ma, C. W. et al. Time-resolved transient electroluminescence measurements of emission from DCM-doped Alq_3 layers. *Chem. Phys. Lett.* **397**, 87–90 (2004).
41. Kim, Y.-H., Wolf, C., Cho, H., Jeong, S.-H. & Lee, T.-W. Highly efficient, simplified, solution-processed thermally activated delayed-fluorescence organic light-emitting diodes. *Adv. Mater.* **28**, 734–741 (2016).
42. Shim, W. et al. Multifunctional cantilever-free scanning probe arrays coated with multilayer graphene. *Proc. Natl Acad. Sci. USA* **109**, 18312–18317 (2012).
43. Gao, A. et al. Printable $CsPbBr_3$ perovskite quantum dot ink for coffee ring-free fluorescent microarrays using inkjet printing. *Nanoscale* **12**, 2569–2577 (2020).
44. Deng, W. et al. Organometal halide perovskite quantum dot light-emitting diodes. *Adv. Funct. Mater.* **26**, 4797–4802 (2016).
45. Sun, C. et al. High-performance large-area quasi-2D perovskite light-emitting diodes. *Nat. Commun.* **12**, 2207 (2021).

Methods

Synthesis of perovskite nanocrystals. To form a clear transparent precursor solution, 0.1 mmol FABr (Dyesol) or a mixture of FABr and GABr (Dyesol) (molar ratio of 0.875:0.125) with 0.2 mmol $PbBr_2$ (Aldrich) were dissolved in 0.5 ml *N*,*N*-dimethylformamide (DMF). Then, 0.15 ml of the precursor solution was added dropwise to a mixture of 5 ml toluene, 2 ml 1-butanol, 0.3 ml oleic acid and 24.2 µl *n*-decylamine with vigorous stirring. The solution turned yellow-green immediately. After mixing for 10 min, the solution was transferred to a falcon tube and then centrifuged at 12,000 r.p.m. for 10 min. The aggregated large particles were collected and then redispersed in 1 ml toluene. The final solution was obtained by collecting the supernatant solution after centrifuging for a second time at 3,750 r.p.m. for 10 min. The sequential centrifuging process removed the excess organic ligands that did not interact with the PNCs.

Preparation of precursors for perovskite polycrystalline bulk films. A clear transparent precursor solution with a concentration of 30.0 wt% was prepared by dissolving FABr and $PbBr_2$ in DMSO (the molar ratio of FABr/$PbBr_2$ was 1.1:1).

PeLED fabrication and characterization. First, 70 nm ITO patterned glasses were cleaned by sonication in acetone and isopropanol for 15 min, respectively. After evaporating the residual solvent, the glasses were treated with ozone for 10 min. Then, Buf-HIL, consisting of a 1:1 (wt/wt) poly(3,4-ethylenedioxythiophene):poly(styrene sulfonate) (PEDOT:PSS) and perfluorinated ionomer, were spin-coated to a layer thickness of 40 nm. After baking at 150 °C for 30 min, samples were transferred to a glove box with N_2 conditions for the PNC film fabrication. Printed PNC and perovskite polycrystalline films were fabricated by bar coating followed by tilting of the substrates at an angle of >50° with respect to the surface. Spin-coated PNC films were fabricated by spin coating the PNC solutions at 1,000 r.p.m. for 60 s, whereas spin-coated polycrystalline films were fabricated by dropping 3–4 droplets of chloroform solvent onto the quasi-film of the precursor solution during spinning (nanocrystal pinning was conducted after spinning at 3,000 r.p.m. for 30 s). For the $FA_{0.875}GA_{0.125}PbBr_3$ PNC-PeLEDs, we spin-coated TBTB dissolved in toluene onto the perovskite emitting layer to create a 5-nm-thick layer. Then, the samples were moved to a high-vacuum evaporation chamber and a 50-nm-thick layer of TPBI, 1-nm-thick layer of LiF and 100-nm-thick layer of Al were sequentially deposited as the cathode. The devices were encapsulated to maintain N_2 conditions and exclude H_2O and O_2. A Keithley 236 device was used as source measurement unit and a Minolta CS 2000 spectroradiometer was used to measure the luminance characteristics of the PeLEDs.

Time-correlated single-photon-counting measurement. PL lifetime was measured using a FluoTime 300 spectrometer. A picosecond-pulse laser head (LDH-P-C-405B, PicoQuant) was used to excite the samples at a laser wavelength of 405 nm. A photon-counting detector (PMA Hybrid 07) and time-correlated single-photon-counting module (PicoHarp, PicoQuant) were used to detect the PL decay and calculate the PL lifetimes of samples.

Photoluminescence and photoluminescence quantum efficiency measurement. PL spectra were recorded using a JASCO FP8500 spectrofluorometer. To measure the PLQE of the PNC solutions, the same spectrofluorometer was equipped with a 100-nm integrating sphere. PLQE values were calculated using Jasco SpectraManager II software.

Transmission electron microscopy measurement. Transmission electron microscopy images of PNCs were collected using a JEOL-JEM 2100F microscope operating at an acceleration voltage of 200 kV.

Data availability

The data that support the plots within this paper and other findings of this study are available from the corresponding author upon reasonable request.

Acknowledgements

This work was supported by a National Research Foundation of Korea (NRF) grant, funded by the Korean government (MSIT; NRF-2016R1A3B1908431). This research was also supported by the Creative Materials Discovery Program through the NRF, funded by the Ministry of Science and ICT (2018M3D1A1058536).

Author contributions

T.-W.L. designed and supervised the study, analysed the data and prepared the manuscript. Y.-H.K. and J.P. designed the study, performed experiments, analysed the data and prepared the manuscript. S.K. and J.S.K. fabricated the perovskite polycrystal and PNC films. S.-H.J. helped with transient EL measurements. H.X. and B.H. performed and analysed magnetic field-dependent measurements. All authors discussed the results and commented on the manuscript.

Competing interests

The authors declare no competing interests.

Additional information

Supplementary information The online version contains supplementary material available at https://doi.org/10.1038/s41565-022-01113-4.

Correspondence and requests for materials should be addressed to Tae-Woo Lee.

Peer review information *Nature Nanotechnology* thanks Mingjian Yuan, Haizheng Zhong and the other, anonymous, reviewer(s) for their contribution to the peer review of this work.

Reprints and permissions information is available at www.nature.com/reprints.